**Preprints, Joint 9th IFAC Symposium on Robust Control Design and 2nd IFAC Workshop on Linear Parameter Varying Systems Florianopolis, Brazil, September 3-5, 2018**

# Comparison of Parameter-Varying Decoupling Based Control Schemes for a Quadrotor

**Thomas T.R. van de Wiel** *, **Roland Tóth** *, **Vsevolod I. Kiriouchine** *

* *Eindhoven University of Technology, Eindhoven, The Netherlands (e-mail: t.t.r.van.de.wiel@student.tue.nl; r.toth@tue.nl; v.i.kiriouchine@alumnus.tue.nl).*

**Abstract:** This paper presents and compares approaches to the design of flight controllers for quadrotor helicopters based on *Linear Parameter-Varying* (LPV) decoupling techniques. It is shown that parameter-varying decoupling makes it possible to use SISO LTI control design to address all degrees of motion freedom subject to high-speed maneuvers that require large pitch and roll angles. Specifically a decoupling method based on local linearizations (gain-scheduling decoupling) is compared to a global scheduling-dependent decoupling method inspired by computed-torque control, where the scheduling is based on the tilt angels of the drone. Based on an extensive simulation study, it is demonstrated that such a relatively simple control architecture can achieve significantly better performance than LTI control. Conceptually, the presented techniques can be used for the design of control schemes for aircraft and missiles.

*Keywords:* Linear Parameter-Varying systems; decoupling; quadrotor.

## 1. INTRODUCTION

Recently, *unmanned aerial vehicles* (UAVs) have become popular due to their maneuverability, relatively cheap design and increasing sensor and computational capabilities to realize fully autonomous execution of tasks from transportation to surveillance (Mellinger et al. (2012); Bachrach et al. (2011); Mahony et al. (2012)). Quadrotors are a type of UAV with four rotors placed on the tips of a cross-shaped structure. Flight control design for quadrotors is often based on linearized dynamics of the system around hovering where all degrees of freedom of the body translation and pose become naturally decoupled. This makes it possible to design *single-input single-output* (SISO) controllers by standard loop-shaping and PID techniques to achieve stabilization and motion control of the vehicle (Mahony et al. (2012)). However, in case of aggressive maneuvers where pitch and roll angels substantially deviate from the hovering pose, non-linear coupling effects appear which quickly deteriorate the performance of the flight controller. To address this problem, various approaches have been applied, starting from switched control architectures (including gain-scheduling, (see e.g (Mellinger et al. (2012)) where the local controllers are designed for a specific operating envelope up to full-scale non-linear controllers designed based on integral back-stepping (Bouabdallah and Siegwart (2007)) and sliding mode design (Xu and Özgüner (2006)). While these approaches give elegant mathematical solutions to the underlying control problem, generally it is difficult to tune their performance in practice and they require a significant step in implementation from the simple decoupled linear architecture of standard flight controllers.

To re-utilize advanced methods of performance shaping available in the linear case, the underlying non-linearities of the motion dynamics can also be captured in and represented by a *linear parameter-varying* (LPV) model (see Tóth (2010)). In an LPV representation, the dynamical mapping between inputs and outputs is linear while the mapping itself depends on a time-varying and online measurable scheduling variable. Thus, non-linearities in the original system can be represented by variations in the scheduling signal. In case of the quadrotor, such scheduling variables can be constructed based on the non-linear relationships introduced by the body pose in the motion dynamics. In Cisneros et al. (2016); Serirojanakul and Wongsaisuwan (2012); Rangajeeva and Whidborne (2011) optimal LPV *multi-input multi-output* (MIMO) controllers have been designed and applied to quadrotor motion control. While such approaches benefit from the toolchain of *optimal control design* to assist performance tuning, they require significant expertise to be applied.

In this paper, we would like to demonstrate the use of the LPV concept for motion control of quadrotors from a different perspective, which can be seen as a direct extension of the simplified decoupled LTI design, not requiring the solution of an optimal MIMO synthesis problem. Specifically, we compare two scheduling-dependent decoupling methods that enable us to use decoupled PID control of the dynamics. We develop a local linearizations based decoupling of the dynamics and also a global decoupling solution, which can be directly used with a controller tuned for hovering conditions. Compared to various gain-

⋆ This work has received funding from the European Research Council (ERC) under the European Union's Horizon 2020 research and innovation programme (grant agreement No. 714663).

scheduling solutions presented for quadrotors (Mellinger et al. (2012)), we do not design a controller separately for specific operating points, but our contribution is in the extension of the concept of LTI decoupling (Franklin (2015)) for non-linear systems represented by an LPV model. We intend to show with this paper that LPV control can also be applied in a simple manner to solve practical motion control problems.

The paper is organized as follows: In Section 2, a non-linear dynamic motion model of a quadrotor is derived and the effects of coupling terms on the local linearizations of the dynamics are highlighted. In Section 3, local and global LPV decoupling schemes are introduced together with the corresponding control structure and their implementation is discussed. This is followed by a detailed simulation study in Section 4, where the decoupling schemes are compared and their performance during agile maneuvering is demonstrated. Finally, conclusions on the presented results are drawn in Section 5.

## 2. QUADROTOR MOTION MODEL

### *2.1 System Dynamics*

Fig. 1 shows the drone configuration that is considered in this paper. The state and input variables are defined as

$$X = [x\ y\ z\ V_x\ V_y\ V_z\ \phi\ \theta\ \psi\ p\ q\ r]^\top, \tag{1a}$$

$$u = [T\ \tau_x\ \tau_y\ \tau_z]^\top. \tag{1b}$$

$x$, $y$, $z$, $V_x$, $V_y$, $V_z$ are the positions and velocities in the inertial frame; $\phi$, $\theta$, $\psi$ are the Tait-Bryan rotational angles; $p$, $q$, $r$ are the rotational velocities of the body. The equations of motion are given by (2) as derived in Mahony et al. (2012); Kiriouchine (2017):

$$\dot{X} = \begin{bmatrix} \dot{x} \\ \dot{y} \\ \dot{z} \\ \dot{V}_x \\ \dot{V}_y \\ \dot{V}_z \\ \dot{\phi} \\ \dot{\theta} \\ \dot{\psi} \\ \dot{p} \\ \dot{q} \\ \dot{r} \end{bmatrix} = \begin{bmatrix} V_x \\ V_y \\ V_z \\ -(\sin\phi\cdot\sin\psi + \cos\phi\cdot\cos\psi\cdot\sin\theta)\frac{T}{m} \\ -(\cos\phi\cdot\sin\psi\cdot\sin\theta - \cos\psi\cdot\sin\phi)\frac{T}{m} \\ -(\cos\phi\cdot\cos\theta)\frac{T}{m} + g \\ p + \sin\phi\cdot\tan\theta\cdot q + \cos\phi\cdot\tan\theta\cdot r \\ \cos\phi\cdot q - \sin\phi\cdot r \\ \frac{\sin\phi}{\cos\theta}\cdot q + \frac{\cos\phi}{\cos\theta}\cdot r \\ \frac{I_y - I_z}{I_x}\cdot q\cdot r + \frac{\tau_x}{I_x} \\ \frac{I_z - I_x}{I_y}\cdot p\cdot r + \frac{\tau_y}{I_y} \\ \frac{I_x - I_y}{I_z}\cdot p\cdot q + \frac{\tau_z}{I_z} \end{bmatrix}, \tag{2}$$

where $T$ denotes the overall thrust (in $z$-direction), $\tau_i$ and $I_i$ the applied torque and the moment of inertia around axis $i \in \{x, y, z\}$. Note that an isomorphic mapping $f$ is used for the conversion of torque to propeller thrust, i.e. $f : \tau_i \xrightarrow{\sim} \{T_j\}$, $j \in \{1, 2, 3, 4\}$.

### *2.2 Linearized State-Space Model*

The non-linear dynamics of (2) can be linearized around chosen operating points by making use of a first order Taylor expansion:

$$\dot{X} = f(X, u) \approx f(X_0, u_0) + A\,(X - X_0) + B\,(u - u_0), \tag{3}$$

where the state-space matrices $A$ and $B$ are defined as

$$A = \frac{\partial f}{\partial X}\Big|_{X=X_0, u=u_0} \text{ and } B = \frac{\partial f}{\partial u}\Big|_{X=X_0, u=u_0}. \tag{4}$$

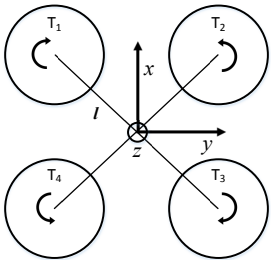


Fig. 1. Top view of the considered quadrotor drone layout. All rotors are placed at equal distance $l$ from the center of gravity and exert a thrust force $T_i$. The origin of the Cartesian, right-rotating (body) coordinate system lies at the center of gravity of the drone.

The desired state $X_0$ is always chosen to be stationary:

$$X_0 = [x_0\ y_0\ z_0\ 0\ 0\ 0\ \phi_0\ \theta_0\ \psi_0\ 0\ 0\ 0]^\top = \mathbb{R}^{12}. \tag{5}$$

Note that this choice causes $f(X_0, u_0)$ in (3) to become 0. Furthermore, the linearization in terms of the obtained matrices $A$ and $B$ is not dependent on $x_0$, $y_0$, $z_0$, but only on $\phi_0$, $\theta_0$, $\psi_0$. To maintain the stationary point, the control torques $u_0$ cannot cause a change in attitude and the overall thrust needs to compensate for gravity, thus

$$u_0 = \Big[\frac{mg}{\cos(\phi)\cos(\theta)}\ 0\ 0\ 0\Big]^\top. \tag{6}$$

For an output equation, we define $C$ such that $y$ contains the state variables corresponding to the measurable altitude and body pose:

$$y = [z\ \phi\ \theta\ \psi]^\top. \tag{7}$$

The linearized state-space model of the plant $G$ is then

$$G \begin{cases} \dot{X}(t) &= A\,X(t) + B\,u(t) \\ y(t) &= C\,X(t) \end{cases}. \tag{8}$$

Expressions for state-space matrices $A$, $B$ and $C$ can be found in Appendix A. Note that the system is a general rotational robotic system of the form

$$D(q)\ddot{q} + C(q, \dot{q})\dot{q} + K(q)q = \tau, \tag{9}$$

where $q$ denotes the vector of state variables and $\tau$ is the actuation input.

### *2.3 Coupling*

A local and a global LPV decoupling scheme are presented as alternatives for the more common LTI approach. When the LTI system is linearized around hover, it follows from inspection of (A.1)-(A.8) that the resulting system is locally decoupled. Decoupling means that each input $u$ only influences its corresponding *degree of freedom* (DOF). Hence, the 4 input, 4 output MIMO system then reduces to 4 separate SISO systems, which greatly simplifies the controller design. When deviating from hover, coupling effects manifest and the performance of a LTI decoupled design based controller (often just tuned for hovering) deteriorates. Local and global LPV schemes will likely perform better under these conditions where the controller is capable to adopt the changes in dynamics. For this reason, the comparison of Section 4 focuses on the coupled regime. Table 1 displays where the coupling between DOFs occurs. The results are obtained by analyzing Bode plots of different linearizations of the 4 input, 4 output MIMO system. Besides the trivial coupling (o) on the main diagonal, coupling exists between:

Table 1. Coupling between the DOFs.

| | **T** | $\tau_x$ | $\tau_y$ | $\tau_z$ |
|---|---|---|---|---|
| z | o | b/c | c | c |
| $\phi$ | | o | c | a/c |
| $\theta$ | | | o | b/c |
| $\psi$ | | | c | o |

a) $\tau_z$-$\phi$ (pure roll, $\phi$)
b) $\tau_x$-$z$ / $\tau_z$-$\theta$ (pure pitch, $\theta$)
c) $\tau_x$-$z$ / $\tau_y$-$z$, $\phi$, $\psi$ / $\tau_z$-$z$, $\phi$, $\theta$ (combined pitch and roll)

Comparing tests can be conducted under the following conditions. Influence of change of

(1) $\tau_x$ on $z$ $(\theta \neq 0)$
(2) $\tau_y$ on $z$, $\phi$ and $\psi$ $(\phi \neq 0 \wedge \theta \neq 0)$
(3) $\tau_z$ on $z$, $\phi$ and $\theta$ $(\phi \neq 0 \wedge \theta \neq 0)$

In order to deal with these coupling effects, we will utilize two types of LPV decoupling schemes. A traditional gain-scheduling based local LPV scheme (LLPV) which uses only angles in the linearization. Hence, angular rates and transient dynamics between the stationary points are ignored. Also, we propose a novel scheme based on a global LPV (GLPV) method that takes into account both angles and angular rates. To make a fair comparison of the introduced GLPV and LLPV schemes, simulation studies are carried out for both small and large steps in the angles. For large angle steps, the angular rates are higher and thus differences between GLPV and LLPV methods should become apparent.

## 3. LPV DECOUPLING SCHEMES

### *3.1 Gain-Scheduling Based Local Decoupling*

The method of gain-scheduling is used to construct the local LPV scheme. From the known local state-space representation in (8), an equivalent transfer matrix $G(s)$ can be calculated as

$$G(s) = \frac{X(s)}{U(s)} = C(sI - A)^{-1}B, \tag{10}$$

where $s \in \mathbb{C}$ is the Laplace variable and $X(s)$, $U(s)$ are the Laplace transforms of $X$ and $u$. Note that $G(s)$ is a 4x4 matrix of transfer functions that maps each input variable ($T$, $\tau_x$, $\tau_y$, $\tau_z$) to one or more output state variables ($z$, $\phi$, $\theta$, $\psi$). In the ideal decoupled case, each input corresponds to only one output, $T-z$, $\tau_x-\phi$, $\tau_y-\theta$, $\tau_z-\psi$. The MIMO system can then be reduced to 4 separate SISO systems. However, due to the characteristics of the system, this is not the case when $\phi_0$, $\theta_0$, $\psi_0$ are not zero. For example, altitude is lost when changing pitch or roll; see Table 1.

The transfer matrix in (10) only consists of second and fourth-order integrators, and can therefore be written as

$$G_p(s) = M_1(\alpha)\,\frac{1}{s^2} + M_2(\alpha)\,\frac{1}{s^4}, \tag{11}$$

with $M_1(\alpha)$ and $M_2(\alpha)$ constant gain matrices dependent on the scheduling variable $\alpha = [\phi_0, \theta_0]^\top$. Note that for the chosen output (7), the resulting dynamics of $\dot{z}$, $\dot{\phi}$, $\dot{\theta}$ and $\dot{\psi}$ do not depend on $\psi$. Hence $\psi_0$ is not used as a scheduling variable. To achieve perfect decoupling, we would like to map the 4x4 MIMO system (11) to 4 double integrator SISO systems and scale the control signals to account for the thrust mapping in the actual plant. To this end, the decoupling filter $T_p(s)$ is defined as

$$T_p(s) = T_1(\alpha) + \frac{1}{s^2}\,T_2(\alpha), \tag{12}$$

with $T_1(\alpha)$ and $T_2(\alpha)$ again constant matrices depending on $\alpha$. We now impose that

$$G_p(s)\,T_p(s) = I\,\frac{1}{s^2}, \tag{13}$$

which leads to the following system of matrix equations

$$\underbrace{\begin{bmatrix} M_1(\alpha) & 0 \\ M_2(\alpha) & M_1(\alpha) \\ 0 & M_2(\alpha) \end{bmatrix}}_{\tilde{M}_p} \underbrace{\begin{bmatrix} T_1(\alpha) \\ T_2(\alpha) \end{bmatrix}}_{\tilde{T}_p} = \underbrace{\begin{bmatrix} I \\ 0 \\ 0 \end{bmatrix}}_{\tilde{S}}. \tag{14}$$

The scaling matrices $T_1$ and $T_2$ can now be calculated by solving the system of matrix equations in (14):

$$\tilde{T}_p = (\tilde{M}_p^\top \tilde{M}_p)^{-1} \tilde{M}_p^\top \tilde{S}. \tag{15}$$

The proposed feedback control loop based on the decoupling filter $T_p(s)$ is displayed in Fig. 2. Note that the matrices $T_1(\alpha)$ and $T_2(\alpha)$ are selected online from a lookup table based on the current operating point of the system. The controllers addressing the decoupled SISO dynamics can be of any desired type and are designed according to standard feedback controller design methods, see e.g. Franklin (2015). In this paper, a simple PID controller is used.

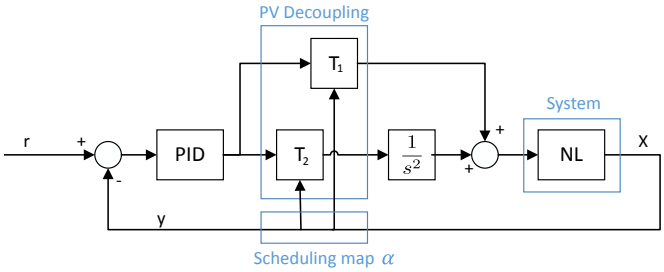


Fig. 2. Local LPV decoupling using gain-scheduling. The controller consists of four PID-controllers, all designed for a $\frac{1}{s^2}$ system with standard loop shaping techniques. The blocks $T_1$ and $T_2$ denote the parameter-varying decoupling. The scheduling map selects the appropriate values depending on the scheduling variable $\alpha$.

### *3.2 Parameter-Varying Global Decoupling*

The disadvantage of the presented LLPV decoupling scheme is that it ignores non-linear dynamics between changing operating points. Additionally, the lookup table may require dedicated memory. To overcome these issues, a signal substitution based scheme in a form similar to *computed torque control* (CTC) is proposed to construct a global LPV decoupling. The system in (10) can be rewritten to

$$u = M(\eta)\ddot{\eta} + V(\eta, \dot{\eta}), \tag{16}$$

where $u$ is the vector of actuation inputs, and $\eta$ is the part of the state $X$:

$$\eta = [z\ \phi\ \theta\ \psi]^\top. \tag{17}$$

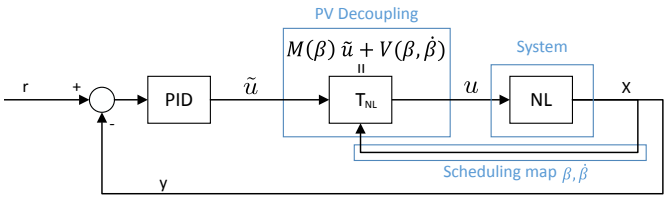


Fig. 3. Global LPV decoupling based on computed torque control. The controller consists of four PID-controllers, all designed for a $\frac{1}{s^2}$ system. The block $T_{\mathrm{NL}}$ denotes the global LPV decoupling.

For the particular system at hand, the dynamics can be written as

$$u = M(\beta)\ddot{\eta} + V(\beta, \dot{\beta}), \tag{18}$$

with $\beta$ a scheduling variable defined as

$$\beta = [\phi\ \theta\ \psi]^\top. \tag{19}$$

A linearizing transformation of the system in (18) is now given by

$$u = M(\beta)\tilde{u} + V(\beta, \dot{\beta}), \tag{20}$$

with $\tilde{u}$ the unscaled control signal resulting from the 4 SISO PID controllers. By applying (20) on (18), the system becomes linear and decoupled, resulting in

$$\tilde{u} = \ddot{\eta}. \tag{21}$$

In Kiriouchine (2017), a full derivation of the matrices $M(\beta)$ and $V(\beta, \dot{\beta})$ is given for the quadrotor drone system of (2). The obtained global LPV decoupling based control structure is displayed in Fig. 3.

## 4. SIMULATION STUDY

### *4.1 General remarks*

The presented decoupled system descriptions have been constructed and implemented in Matlab/Simulink. For comparison purposes, pure LTI control was also implemented by taking the LLPV scheme and setting the scheduling variable $\alpha = [0\ 0]^\top$. In terms of implementation, the following remarks are in place:

- Parameter values are chosen to match those of the Parrot AR Drone 2.0 and can be found in Table 2;
- The control input is saturated to the maximum available thrust and torque of this platform;
- Inspection of the transfer matrices showed that fourth order integrator terms are not present for yaw. In order to avoid superfluous integrators for yaw in the local LPV decoupling, this channel is set to zero;
- A saturation of +/- 2 is placed on the second order integrator of the $T_2$ channel of Fig. 2;
- Gravity feedforward is already accounted for in the GLPV scheme. For LTI and LLPV, it is added to the control loop according to (6).

This section summarizes all simulation results by means of tracking plots, *root-mean square error* (RMS) values, and maximum tracking error. The chosen reference input are step responses for the angles corresponding to the input torques considered. Both large and small steps are considered. All numerical results are summarized in tabular form. Note that the first six seconds of each simulation are used to attain the starting angles and to reach steady-state. The lookup tables $T_1(\alpha)$ and $T_2(\alpha)$ of the local LPV scheme have a resolution of 1° (although all resolutions below 5° yield similar results). Plots are only given for variables displaying interesting behavior. Small step plots are omitted since the behavior is qualitatively seen similar to the large steps; quantitative results can be found in the supplied tables. The angular controllers are simple PD-controllers with bandwidth of approximately 50, 40 and 10 Hz for $\phi$, $\theta$ and $\psi$ respectively. For the height controller, the bandwidth is roughly 7 Hz and an integrator is added. To make a fair comparison, all three schemes use the same controller tuning.

Table 2. Parameters of the Parrot AR Drone 2.0 (Jeurgens (2017)).

| Parameter | Symbol | Value | Unit |
|---|---|---|---|
| mass | $m$ | 0.429 | kg |
| inertia $x$-axis | $I_x$ | 0.00224 | kg m$^2$ |
| inertia $y$-axis | $I_y$ | 0.00299 | kg m$^2$ |
| inertia $z$-axis | $I_z$ | 0.00480 | kg m$^2$ |
| max. total thrust | $T_{\max}$ | 7.76 | N |
| max. torque $x$-axis | $\tau_{x,\max}$ | 0.43 | Nm |
| max. torque $y$-axis | $\tau_{y,\max}$ | 0.43 | Nm |
| max. torque $z$-axis | $\tau_{z,\max}$ | 0.11 | Nm |
| max. angles to just compensate for gravity | $\sqrt{\phi^2+\theta^2}_{\max}$ | 57 | ° |

### *4.2 Decoupling of $\tau_x$-$z$*

For pitch angle $\theta = 40°$, the decoupling of $z$ with $\tau_x$ is investigated. The trajectory of $\phi$ can be seen in Fig. 4. Roll tracking behavior is nearly identical for the local and global LPV schemes. The standard LTI controller displays a constant offset. LLPV and GLPV show good tracking performance. The tracking of $z$ for the roll trajectory of Fig. 4 can be seen in Fig. 5. The LLPV method gives a smaller tracking error than LTI. However, the GLPV performs significantly better than LLPV. Pitch and yaw are unaffected by a change in $\tau_x$ as highlighted in Table 1. The experiment has been repeated for a small step trajectory, which makes steps of +5°, -5°, -5°, +5° at the same time instances as the large step trajectory in Fig. 4. Tables 3 and 4 summarize the results of the decoupling of $\tau_x$-$z$. The tables compare the ratios of both RMS and maximum error of different controllers; columns compare GLPV-LTI, GLPV-LLPV and LLPV-LTI respectively. The most advanced decoupling strategy is always in the numerator. A value smaller than one thus denotes that the advanced scheme results in better performance. GLPV yields better performance than LTI and LLPV. The larger the steps, the better the performance of GLPV compared to LLPV because the non-linearities w.r.t. the angular rates are taken into account. LLPV gives better results than nominal LTI based control; for small steps, the performance difference is largest. As a conclusion, GLPV is the preferred decoupling scheme. LLPV and LTI yield similar performance.

### *4.3 Decoupling of $\tau_y$ - $z$, $\phi$, $\psi$*

For $\phi = 40°$, the coupling of $z$, $\phi$ and $\psi$ with $\tau_y$ is investigated. The trajectory of $\theta$ is the same as for $\phi$. Pitch tracking behavior is virtually identical to Fig. 4, hence the plot is omitted. The tracking of $z$, $\phi$ and $\psi$

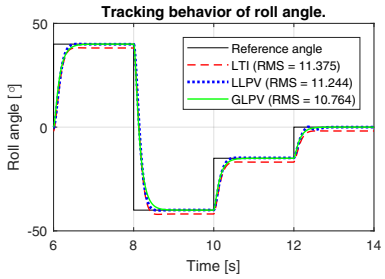


Fig. 4. Large step $\phi$ trajectory for analyzing the influence of $\tau_x$.

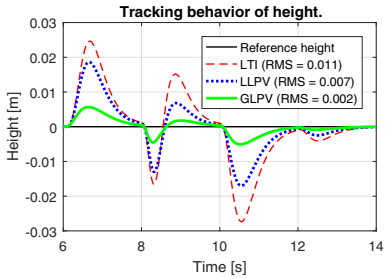


Fig. 5. $z$ tracking behavior for the roll trajectory of Fig. 4.

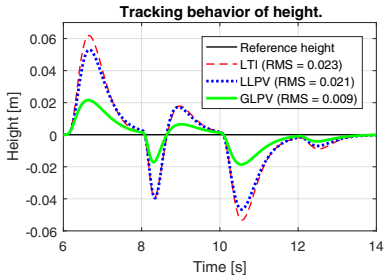


Fig. 6. $z$ tracking for the pitch trajectory similar to Fig. 4.

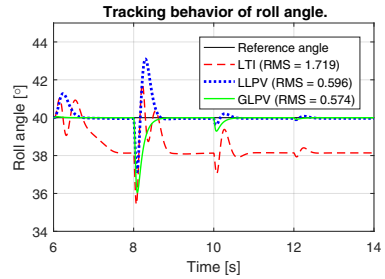


Fig. 7. $\phi$ tracking for the pitch trajectory similar to Fig. 4.

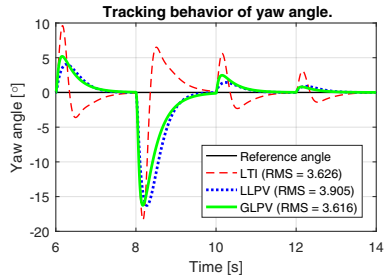


Fig. 8. $\psi$ tracking for the pitch trajectory similar to Fig. 4.

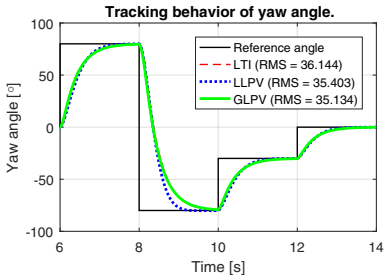


Fig. 9. Large step $\psi$ trajectory for analyzing the influence of $\tau_z$.

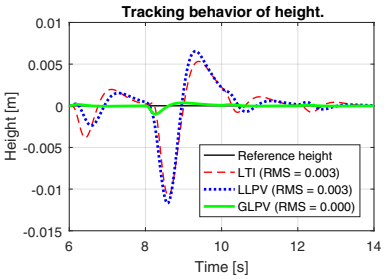


Fig. 10. $z$ tracking for the yaw trajectory of Fig. 9.

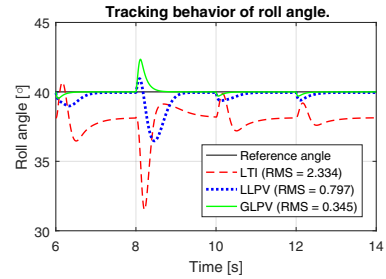


Fig. 11. $\phi$ tracking for the yaw trajectory of Fig. 9.

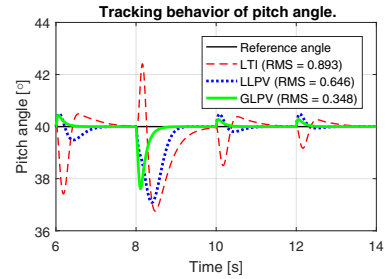


Fig. 12. $\theta$ tracking for the yaw trajectory of Fig. 9.

for the pitch trajectory similar to Fig. 4 can be seen in Fig. 6, 7, and 8 respectively. The same procedure has been repeated for small steps, similar to the decoupling of $\tau_x - z$. Tables 5 and 6 summarize the results of the coupling analysis $\tau_y$-$z$, $\phi$, $\psi$. GLPV based decoupling generally gives better results than the LLPV scheme in terms of average error and in terms of maximum error. Both the GLPV and the LLPV schemes give better performance than the nominal LTI scheme.

### *4.4 Decoupling of $\tau_z$ - $z$, $\phi$, $\theta$*

For $\phi = \theta = 40°$, the coupling of $z$, $\phi$, $\theta$ and $z$ with $\tau_z$ is investigated. The trajectory of $\psi$ can be seen in Fig. 9. Yaw tracking behavior is nearly identical for all controllers. The tracking of $z$, $\phi$ and $\theta$ for the yaw trajectory of Fig. 9 can be seen in Fig. 10, 11, and 12 respectively. The same procedure has been repeated for small steps, similar to the previous sections. Tables 7 and 8 summarize the results of the coupling $\tau_z$-$z$, $\phi$, $\theta$. The global LPV scheme yields significantly better results than LTI. Also w.r.t. LLPV, GLPV yields better performance. The LLPV scheme has fluctuating performance improvement w.r.t. the LTI approach; for some DOFs LLPV is better, for others LTI is preferred. No clear preference between nominal LTI control and local LPV decoupling based control can be stated. As an overall conclusion, the GLPV scheme is preferred.

### *4.5 Model Sensitivity*

Since the presented decoupling schemes are based on a dynamic model and the corresponding model parameters, it is useful to assess the sensitivity of the controller performance to parameter deviations. In the equations of motion in (2), one can see that only the mass and the moments of inertia play a role in the model. Therefore, our sensitivity analysis will only consider $m$, $I_x$, $I_y$ and $I_z$. It is relatively simple to accurately determine the mass, hence only small deviations of -10, +10 and +20% are considered. Inertia is investigated for bigger deviations of -20, +20 and +100% as it is more difficult to obtain an accurate estimate. Note that +0% denotes a perfect match between model and reality; +10% denotes that the actual parameter value is 10% higher than the modeled value. The percentage change thus always denotes *how the actual value changed w.r.t. the modeled value.* It is investigated how the RMS average error ratios in Tables

Table 3. Average coupling error $\tau_x$-$z$.

| Step | DOF | $\frac{\text{RMS}_{\text{GLPV}}}{\text{RMS}_{\text{LTI}}}$ | $\frac{\text{RMS}_{\text{GLPV}}}{\text{RMS}_{\text{LLPV}}}$ | $\frac{\text{RMS}_{\text{LLPV}}}{\text{RMS}_{\text{LTI}}}$ |
|---|---|---|---|---|
| small | $z$ | 0.22 | 0.53 | 0.43 |
| large | $z$ | 0.22 | 0.33 | 0.67 |

Table 4. Maximum coupling error $\tau_x$-$z$.

| Step | DOF | $\frac{e_{\text{max,GLPV}}}{e_{\text{max,LTI}}}$ | $\frac{e_{\text{max,GLPV}}}{e_{\text{max,LLPV}}}$ | $\frac{e_{\text{max,LLPV}}}{e_{\text{max,LTI}}}$ |
|---|---|---|---|---|
| small | $z$ | 0.16 | 0.48 | 0.32 |
| large | $z$ | 0.21 | 0.30 | 0.68 |

Table 5. Average coupling error $\tau_y$-$z$, $\phi$, $\psi$.

| Step | DOF | $\frac{\text{RMS}_{\text{GLPV}}}{\text{RMS}_{\text{LTI}}}$ | $\frac{\text{RMS}_{\text{GLPV}}}{\text{RMS}_{\text{LLPV}}}$ | $\frac{\text{RMS}_{\text{LLPV}}}{\text{RMS}_{\text{LTI}}}$ |
|---|---|---|---|---|
| small | $z$ | 0.49 | 0.65 | 0.76 |
| | $\phi$ | 0.00 | 0.23 | 0.02 |
| | $\psi$ | 0.55 | 0.49 | 1.12 |
| large | $z$ | 0.38 | 0.43 | 0.89 |
| | $\phi$ | 0.33 | 0.96 | 0.35 |
| | $\psi$ | 1.00 | 0.93 | 1.08 |

Table 6. Maximum coupling error $\tau_y$-$z$, $\phi$, $\psi$.

| Step | DOF | $\frac{e_{\text{max,GLPV}}}{e_{\text{max,LTI}}}$ | $\frac{e_{\text{max,GLPV}}}{e_{\text{max,LLPV}}}$ | $\frac{e_{\text{max,LLPV}}}{e_{\text{max,LTI}}}$ |
|---|---|---|---|---|
| small | $z$ | 0.46 | 0.63 | 0.73 |
| | $\phi$ | 0.01 | 0.48 | 0.02 |
| | $\psi$ | 0.45 | 0.55 | 0.81 |
| large | $z$ | 0.35 | 0.41 | 0.86 |
| | $\phi$ | 0.86 | 1.28 | 0.68 |
| | $\psi$ | 0.89 | 1.00 | 0.89 |

Table 7. Average coupling error $\tau_z$-$z$, $\phi$, $\theta$.

| Step | DOF | $\frac{e_{\text{max,GLPV}}}{e_{\text{max,LTI}}}$ | $\frac{e_{\text{max,GLPV}}}{e_{\text{max,LLPV}}}$ | $\frac{e_{\text{max,LLPV}}}{e_{\text{max,LTI}}}$ |
|---|---|---|---|---|
| small | $z$ | 0.48 | 0.21 | 2.31 |
| | $\phi$ | 0.04 | 0.48 | 0.08 |
| | $\theta$ | 0.84 | 0.50 | 1.68 |
| large | $z$ | 0.07 | 0.07 | 1.09 |
| | $\phi$ | 0.15 | 0.43 | 0.34 |
| | $\theta$ | 0.39 | 0.54 | 0.72 |

Table 8. Maximum coupling error $\tau_z$-$z$, $\phi$, $\theta$.

| Step | DOF | $\frac{e_{\text{max,GLPV}}}{e_{\text{max,LTI}}}$ | $\frac{e_{\text{max,GLPV}}}{e_{\text{max,LLPV}}}$ | $\frac{e_{\text{max,LLPV}}}{e_{\text{max,LTI}}}$ |
|---|---|---|---|---|
| small | $z$ | 0.56 | 0.22 | 2.58 |
| | $\phi$ | 0.13 | 0.52 | 0.25 |
| | $\theta$ | 1.04 | 0.56 | 1.85 |
| large | $z$ | 0.09 | 0.09 | 1.08 |
| | $\phi$ | 0.28 | 0.66 | 0.42 |
| | $\theta$ | 0.74 | 0.82 | 0.90 |

3, 5 and 7 change upon changing the model parameters. In line with previous findings, the performance of pure LTI control is significantly worse than global LPV decoupling based control, and generally speaking worse than local LPV decoupling. Therefore, the results for LTI control are omitted and we will only consider the ratio of GLPV-LLPV. Fig. 13 displays the ratio $\frac{\text{RMS}_{\text{GLPV}}}{\text{RMS}_{\text{LLPV}}}$ w.r.t. benchmark data in which model parameters correspond to the actual parameter values. A value lower than 1 denotes that the global decoupling based controller performs better than the local LPV scheme for the DOF corresponding to the data point. For each data point, it is indicated whether the ratio increased, decreased or remained the same w.r.t. the benchmark data. The smaller the ratio, the better the performance of the global LPV scheme w.r.t. the local method. An increased data point value means the corresponding DOF is more sensitive to modeling errors for the global scheme than for the local one.

From Fig. 13, one can conclude that GLPV yields better performance than LLPV for almost all considered DOFs, even in circumstances where the mass and the moments of inertia are respectively between -10 and +20% and -20 and +100% off from the real value. On average, the global LPV based decoupling scheme results in a factor 2 performance improvement w.r.t. the local scheme. The cases where LLPV yields better performance than GLPV are caused by dynamical variations of the system that are critical in the cancellation scheme of (20). Since the global scheme relies on more accurate model information than the local scheme to improve performance, it loses ground w.r.t. the local scheme as the variations increase. There are critical combinations for which the global scheme even performs worse than the local one. As a rule of thumb, the global decoupling scheme is advised in case of no more than ±20% of nominal parameter uncertainty.

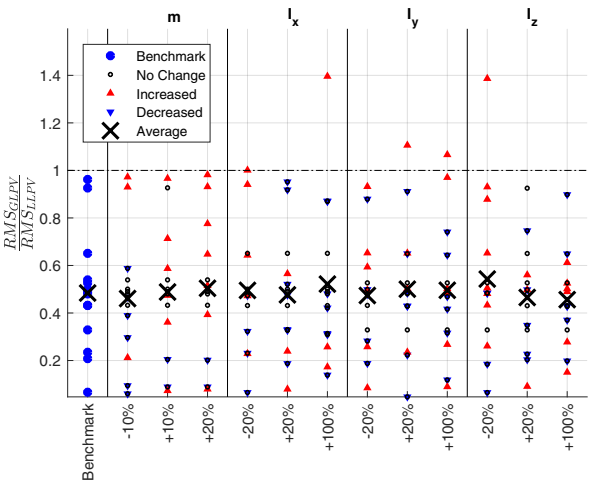


Fig. 13. Sensitivity analysis results for the relative RMS of the GLPV and LLPV decoupling schemes. The columns correspond to variations of $m$, $I_x$, $I_y$ and $I_z$ respectively. Separate points denote individual relative RMS data points, similar to the ones given in the second column of Tables 3, 5 and 7.

## 5. CONCLUSION

In this paper, simple theoretical concepts and detailed simulation results for LPV decoupling based control of a quadrotor drone are presented. Both the proposed local and the global LPV schemes are designed with the purpose of eliminating the coupling between input torques and output DOFs in the system. General analysis of the coupling between degrees of freedom showed that both the global and the local LPV decoupling schemes can improve the performance of a quadrotor drone. Global LPV is generally seen the preferred decoupling scheme.

The model sensitivity analysis showed that even under uncertainty of model parameters, GLPV still performs better than LLPV in most considered circumstances and provides stable operation of the system. In case GLPV is unfeasible for the system at hand, LLPV could be used to improve the performance w.r.t. a LTI-based approach.
The provided decoupling schemes allow the extension of previous designs of flight controllers to address agile maneuvering in drone applications. Conceptually, the proposed technique can be used for a much wider range of applications from motion systems flight and missile control. The hypothesis is that the proposed decoupling technique is applicable to general rotation systems having the form of (9). However, more research is required to verify this hypothesis.

## ACKNOWLEDGEMENTS

The authors would like to thank Xiaoxiao Wen and Mark de Jong for co-developing early versions of the LLPV decoupling scheme and for their contributions to the simulation environment. Arnoud Schmiermann deserves credit for critical revision of the results.

## REFERENCES

Bachrach, A., Prentice, S., He, R., and Roy, N. (2011). RANGE-robust autonomous navigation in GPS-denied environments. *Journal of Field Robotics*, 28, 644–666.

Bouabdallah, S. and Siegwart, R. (2007). Full control of a quadrotor. In *Proc. of the IEEE/RSJ Int. Conf. on Intelligent Robots and Systems*, 153–158. San Diego, USA.

Cisneros, P.S.G., Hoffmann, C., Bartels, M., and Werner, H. (2016). Linear parameter-varying controller design for a nonlinear quad-rotor helicopter model for high speed trajectory tracking. In *Proc. of the American Control Conf.*, 486–491. Boston, MA, USA.

Franklin, Powell, E.N. (2015). *Feedback Control of Dynamic Systems*. Pearson, 7th edition.

Jeurgens, N. (2017). *Identification and Control Implementation of an AR.Drone 2.0*. Master's thesis, Eindhoven University of Technology, The Netherlands.

Kiriouchine, V. (2017). *Sensing and control design for high speed autonomous agile manoeuvring with quad-rotors*. Master's thesis, Eindhoven University of Technology, The Netherlands.

Mahony, R., Kumar, V., and Corke, P. (2012). Multirotor aerial vehicles: Modeling, estimation, and control of quadrotor. *IEEE Robotics & Automation Mag.*, 19, 20–32.

Mellinger, D., Michael, N., and Kumar, V. (2012). Trajectory generation and control for precise aggressive maneuvers with quadrotors. *Int. Journal of Robotics Research*, 31, 664–674.

Rangajeeva, S.L.M.D. and Whidborne, J.F. (2011). Linear parameter varying control of a quadrotor. In *6th Int. Conf. on Industrial and Information Systems*, 483–488. Sri Lanka.

Serirojanakul, A. and Wongsaisuwan, M. (2012). Optimal control of quadrotor helicopter using feedback LPV method. In *9th Int. Conf. on Electrical Engineering/Electronics, Computer, Telecommunications and Information Technology*, 1–4.

Tóth, R. (2010). *Modeling and Identification of Linear Parameter-Varying Systems*. Lecture Notes in Control and Information Sciences, Vol. 403. Springer.

Xu, R. and Özgüner, U. (2006). Sliding mode control of a quadrotor helicopter. In *Proc. of the 45th IEEE Conf. on Decision & Control*, 4957–4962. San Diego, USA.

## Appendix A. STATE-SPACE EQUATIONS

$$A = \begin{bmatrix} 0_{3x3} & I_{3x3} & 0_{3x3} & 0_{3x3} \\ 0_{3x3} & 0_{3x3} & A_{23} & 0_{3x3} \\ 0_{3x3} & 0_{3x3} & A_{33} & A_{34} \\ 0_{3x3} & 0_{3x3} & 0_{3x3} & A_{44} \end{bmatrix}, \tag{A.1}$$

$$A_{33} = \begin{bmatrix} q\, c_\phi t_\theta - r\, s_\phi t_\theta & q\, s_\phi \frac{1}{c_\theta^2} + r\, c_\phi \frac{1}{c_\theta^2} & 0 \\ -r\, c_\phi - q\, s_\phi & 0 & 0 \\ q\, \frac{c_\phi}{c_\theta} - r\, \frac{s_\phi}{c_\theta} & r\, \frac{c_\phi s_\theta}{c_\theta^2} + q\, \frac{s_\phi s_\theta}{c_\theta^2} & 0 \end{bmatrix}, \tag{A.2}$$

$$A_{34} = \begin{bmatrix} 1 & s_\phi t_\theta & c_\phi t_\theta \\ 0 & c_\phi & -s_\phi \\ 0 & \frac{s_\phi}{c_\theta} & \frac{c_\phi}{c_\theta} \end{bmatrix}, \tag{A.3}$$

$$A_{44} = \begin{bmatrix} 0 & r\, \frac{I_y - I_z}{I_x} & q\, \frac{I_y - I_z}{I_x} \\ r\, \frac{I_z - I_x}{I_y} & 0 & p\, \frac{I_z - I_x}{I_y} \\ q\, \frac{I_x - I_y}{I_z} & p\, \frac{I_x - I_y}{I_z} & 0 \end{bmatrix}, \tag{A.4}$$

$$A_{23} = \begin{bmatrix} (A.6b) & (A.6a) & (A.6d) \\ (A.6f) & (A.6c) & (A.6h) \\ (A.6e) & (A.6g) & 0 \end{bmatrix}, \tag{A.5}$$

with

$$-c_\phi c_\theta c_\psi \cdot \frac{T}{m}, \quad \text{(A.6a)} \qquad -(c_\phi s_\psi - s_\phi c_\psi s_\theta) \cdot \frac{T}{m}, \quad \text{(A.6b)}$$

$$-c_\phi c_\theta s_\psi \cdot \frac{T}{m}, \quad \text{(A.6c)} \qquad -(s_\phi c_\psi - s_\psi c_\phi s_\theta) \cdot \frac{T}{m}, \quad \text{(A.6d)}$$

$$s_\phi c_\theta \cdot \frac{T}{m}, \quad \text{(A.6e)} \qquad (s_\phi s_\theta s_\psi + c_\phi c_\psi) \cdot \frac{T}{m}, \quad \text{(A.6f)}$$

$$c_\phi s_\theta \cdot \frac{T}{m}, \quad \text{(A.6g)} \qquad -(c_\phi s_\theta c_\psi + s_\psi s_\phi) \cdot \frac{T}{m}. \quad \text{(A.6h)}$$

Furthermore,

$$B = \begin{bmatrix} 0 & 0 & 0 & 0 \\ 0 & 0 & 0 & 0 \\ 0 & 0 & 0 & 0 \\ -(s_\phi s_\psi + c_\phi s_\theta c_\psi) \cdot \frac{1}{m} & 0 & 0 & 0 \\ -(c_\phi s_\theta s_\psi - s_\phi c_\psi) \cdot \frac{1}{m} & 0 & 0 & 0 \\ -(c_\phi c_\theta) \cdot \frac{1}{m} & 0 & 0 & 0 \\ 0 & 0 & 0 & 0 \\ 0 & 0 & 0 & 0 \\ 0 & 0 & 0 & 0 \\ 0 & \frac{1}{I_x} & 0 & 0 \\ 0 & 0 & \frac{1}{I_y} & 0 \\ 0 & 0 & 0 & \frac{1}{I_z} \end{bmatrix}. \tag{A.7}$$

Finally,

$$C = \begin{bmatrix} 0 & 0 & 1 & 0 & 0 & 0 & 0 & 0 & 0 & 0 & 0 & 0 \\ 0 & 0 & 0 & 0 & 0 & 0 & 1 & 0 & 0 & 0 & 0 & 0 \\ 0 & 0 & 0 & 0 & 0 & 0 & 0 & 1 & 0 & 0 & 0 & 0 \\ 0 & 0 & 0 & 0 & 0 & 0 & 0 & 0 & 1 & 0 & 0 & 0 \end{bmatrix}. \tag{A.8}$$